



## City Research Online

### City, University of London Institutional Repository

---

**Citation:** Sun, Z., Pointz, B. & Bruecker, C. (2016). Transition of a vortex ring measured by 3D scanning Tomo-PIV. Paper presented at the 18th International Symposium on Applications of Laser Techniques to Fluid Mechanics, 4-7 Jul 2016, Lisbon, Portugal.

This is the accepted version of the paper.

This version of the publication may differ from the final published version.

---

**Permanent repository link:** <https://openaccess.city.ac.uk/id/eprint/21653/>

**Link to published version:**

**Copyright:** City Research Online aims to make research outputs of City, University of London available to a wider audience. Copyright and Moral Rights remain with the author(s) and/or copyright holders. URLs from City Research Online may be freely distributed and linked to.

**Reuse:** Copies of full items can be used for personal research or study, educational, or not-for-profit purposes without prior permission or charge. Provided that the authors, title and full bibliographic details are credited, a hyperlink and/or URL is given for the original metadata page and the content is not changed in any way.

---

---

---

City Research Online:

<http://openaccess.city.ac.uk/>

[publications@city.ac.uk](mailto:publications@city.ac.uk)

---

See discussions, stats, and author profiles for this publication at: <https://www.researchgate.net/publication/309638316>

# Transition of A Vortex Ring Visualized by 3D Scanning TomoPIV

Conference Paper · July 2016

CITATIONS

0

READS

128

3 authors, including:



**Zhengzhong Sun**

City, University of London

26 PUBLICATIONS 107 CITATIONS

[SEE PROFILE](#)



**Christoph Brücker**

City, University of London

243 PUBLICATIONS 2,489 CITATIONS

[SEE PROFILE](#)

Some of the authors of this publication are also working on these related projects:



Nature Inspired Flow Sensing and Manipulation [View project](#)



Seal Whisker [View project](#)

# Transition of A Vortex Ring visualized by 3D Scanning TomoPIV

Zhengzhong Sun<sup>1,\*</sup>, Benjamin Pointz<sup>2</sup>, Christoph Bruecker<sup>1</sup>

1: Dept. of Mechanical Engineering & Aeronautics, City University London, UK

2: Institute of Mechanics and Fluid Dynamics, Technical University of Freiberg, Germany

\* Correspondent author: zhengzhong.sun@city.ac.uk

**Keywords:** Vortex ring, Tomographic PIV, Scanning PIV

## ABSTRACT

A vortex ring with piston-based Reynolds number  $Re_p=4650$  is studied experimentally by means of time-resolved scanning tomographic PIV. The present measurement technique provides the so-called 4D flow field, thus enables revealing the vortex ring's transition from laminar to turbulent. The evolution of the ring torus as well as the generation of secondary vortex filaments in transition are first observed through 3D visualization. Analysis on the quantities of the vortex ring, such as circulation and vorticity components, defines the three evolution phases, namely laminar, transition and turbulent. The ring median plane is also examined to provide further insights on flow structure exhibited in transition. The axial vorticity component and radial velocity component are studied respectively and they are found to be organized in a multi-layer concentric-ring pattern. Spectrum analysis on the radial velocity component along the ring core and inner ring where secondary vortical activity happens reveals the dominate wavenumber in transition and broad band of wavenumbers in turbulent phase.

---

## 1. Introduction

The study on vortex ring evolves almost with the history of fluid mechanics. The continuous research efforts on vortex ring can be attributed to the significant transition phenomenon in its lifetime, which allows the study on the classical topics such as flow instability and laminar-turbulence transition. Since the vortex ring is the fundamental structure in the jet flow, more recently, it is being studied due to the ongoing ambition on quiet jetliner. Summarizing the large body of investigations in the literature, the methodologies used in vortex ring study can be classified into numerical and experimental methods. Numerical simulations using direct numerical simulation (DNS) algorithm gives a three-dimensional time resolved visualization of the vortex ring throughout its life time [1]. However, at the earlier stage of experimental study, the vortex ring is mostly visualized by qualitative flow visualization technique, such as dye visualization. Even with the introduction of particle image velocimetry (PIV), the vortex ring can only be studied in a cross-sectional way [2]. The present experimental study will report details of the transition phase of vortex ring taking advantage of the scanning tomographic PIV [3], which

is a recent development of the original scanning PIV [4] and an alternative voxel based tomographic velocimetry [5]. This work is also a continuation of previous work reported in 2012 in the laser conference [3]. The new results to be presented make use of the 3D cross-correlation of the reconstructed intensity volume, which resolves the entire measurement volume. In the next section, the experimental setup and the technical facts of the present scanning PIV experiment are briefly introduced. The result section first provides an overall understanding of the ring evolution through 3D visualization. Focus is later placed at the transition phase while spectrum analysis is also performed to give further insights. Conclusions on the transition process are finally summarized at the end of the paper.

## 2. Experimental setup

The experimental setup has been reported in detail in the paper of Pointz et al.[3], it is thus only briefly discussed. Topview of the setup is sketched conceptually in figure 1, where the alignment of the water tank, cameras and the scanning laser volumes can be seen. The vortex ring is generated through a piston mechanism located at the top of the tank and it propagates towards the bottom of the tank. Three Vision Research Phantom V12.1 high speed cameras constitute the multi-view imaging system for tomography. They are aligned in linear configuration with angular displacement of  $45^\circ$ . Telecentric lenses are used to image particles without perspective effects, and they are critical for the following back-projection procedure in 3D intensity field reconstruction. Since the imaging system remains stationary in the course of measurement, the water tank is traversed upward so that the vortex ring stays in the field of view of the imaging systems. The lift-up speed is set 50 mm/s according to the ring propagation velocity. A Coherent Innova 70 continuous Argon-Ion laser is used for flow illumination. It has 3W power and the output laser beam has a diameter of about 10 mm. The volume illumination is delivered by a drum scanner, where 10 mirrors are aligned over the drum circumference. A laser volume of 50 mm thickness is finally achieved through one cycle of scan. The camera and scanner are synchronized at 1250 Hz. Since each thick volume is formed by every 10 slice scans, the ring is actually sampled at rate of 125 Hz. Neutrally buoyant particles with nominal diameter of 90  $\mu\text{m}$  are used as flow tracers. The major parameters of the experimental setup and the parameters for imaging system is summarized in Table 1.

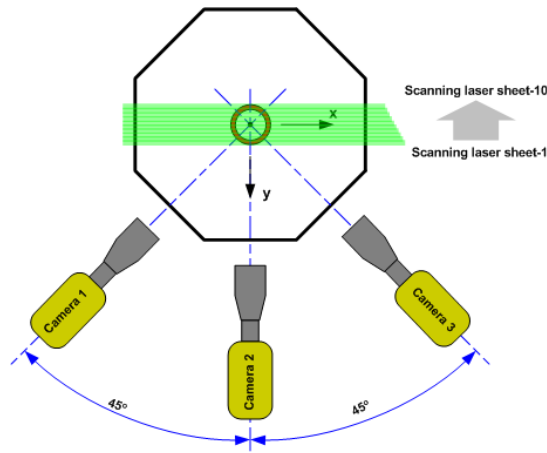


Fig. 1 Top view of the conceptual experimental setup.

Table 1 Parameters for the experimental setup.

Parameter	Quantity
Laser power	$P = 3 \text{ W}$
Laser beam diameter	$d_{\text{beam}} \approx 10 \text{ mm}$
Thickness of scanning laser slice	$t_{\text{slice}} = 8 \text{ mm}$
Displacement between consecutive scanning slices	$\Delta t_{\text{slice}} = 5 \text{ mm}$
Number of scanning slices for each volume	$N = 10$
Thickness of each volume	$t_{\text{vol}} \approx 50 \text{ mm}$
Slice sampling rate	$f_{\text{slice}} = 1250 \text{ Hz}$
Volume sampling rate	$f_{\text{vol}} = 125 \text{ Hz}$
Total number of volumes	$N_{\text{vol}} = 800$
Duration of each volumetric scan	$T_o = 8 \text{ ms}$
Duration of entire measurement	$T = 6.4 \text{ s}$
Numerical aperture	$f_i = 1/16$
Depth of focus	$D = 100 \text{ mm}$
Imaging magnification	$M = 0.2$
Imaging resolution	$R = 0.1 \text{ mm/voxel}$
Tank traverse velocity	$V_{\text{tank}} = 50 \text{ mm/s}$
Particle diameter	$d_p = 90 \text{ }\mu\text{m}$

### 3. Volumetric vector field recovery

The volumetric vector field recovery involves two major steps, namely the 3D intensity field reconstruction and 3D cross-correlation. The former step is based on the back-projection of the particle images captured from the three different angles. The principle and procedure have been

reported extensively in the paper of Pointz [3]. The reconstructed intensity volume has  $700 \times 519 \times 500$  voxels. In the previous work [3], 3D least square matching (LSM) method provided by Dynamic Studio of Dantec Dynamics was used to calculate the particle displacement. However, the flow information at the edge of the volume cannot be recovered. This is due to the insufficient room at the boundary for the cuboid to search the matching particle intensity, which will be overcome in the latest version. 3D cross-correlation is used in the present work for vector calculation, making full use of the entire volume. The final interrogation volume for 3D cross-correlation is  $40 \times 40 \times 40$  voxels with 75% overlap. A total of  $66 \times 48 \times 46$  vectors are achieved in the volume with vector spacing of 10 voxels or 1 mm. The vortex ring returned by previous LSM and present 3D cross-correlation are compared in figure 2. It is apparent that the latter reveals almost the entire ring, despite the front and rear portions are slightly cropped. The parameters of cross-correlation operation and the resulted vector field are summarized in Table 2.

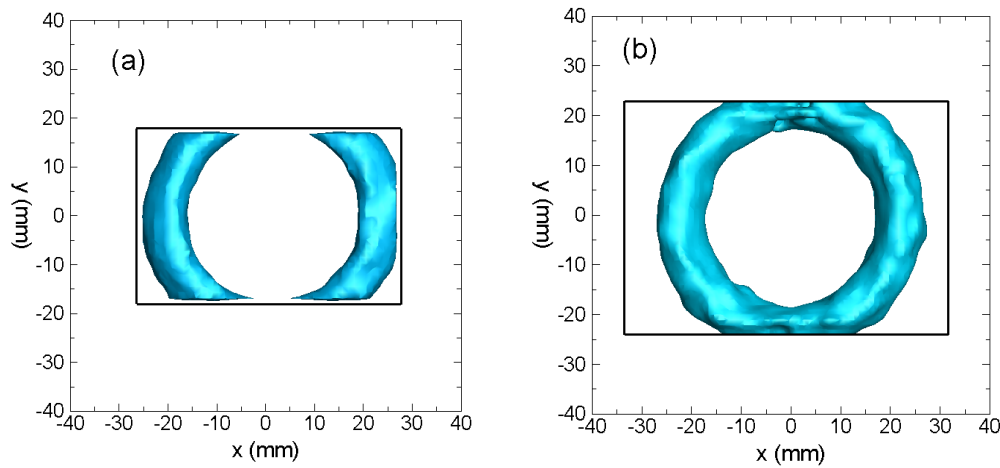


**Fig. 2** Vortex ring returned by 3D LSM (a) and 3D cross-correlation (b), the ring is represented by isosurface of the same vorticity magnitude.

**Table 2** Parameters of volume interrogation

Parameter	Quantity
Voxel volume size	$700 \times 519 \times 500$ voxel
Final interrogation volume	$40 \times 40 \times 40$ voxel
Overlap of interrogation volume	75%
Number of vectors	$66 \times 48 \times 46$
Vector spacing	10 voxel or 1 mm
Resolution	0.1 mm/voxel

### 3. Results and discussions

#### 3.1 Characteristics of vortex ring and its evolution

The characteristics of the vortex ring is first discussed so as to deliver an overall understanding. The ring evolution is determined by its initial property, which largely depends on the generation mechanism. As introduced earlier, the present ring is generated by a piston nozzle. The velocity of the piston along the forward stroke is 155 mm/s. The piston nozzle outlet has a diameter of 30 mm. As a result, the ring has piston-based Reynolds number of  $Re_p=4,650$ . A separate laser visualization experiment reveals that the generated ring has a travelling speed of 50 mm/s, which is later used for the traverse to lift the water tank.

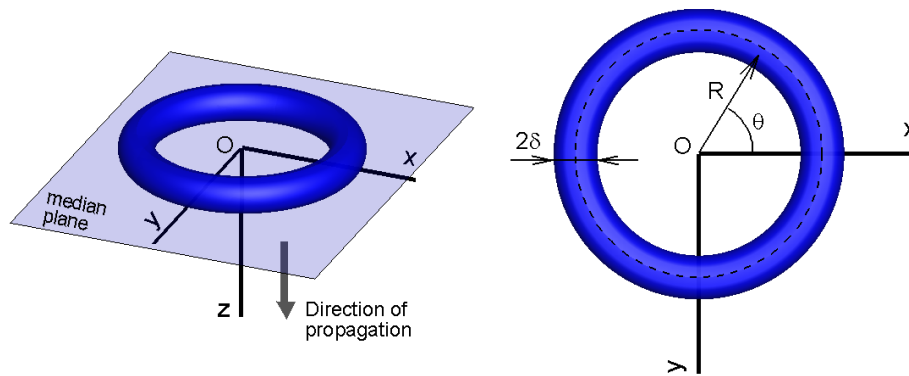


Fig. 3 Cartesian and cylindrical coordinate systems for the vortex ring.

The present scanning PIV experiment resolved the ring evolution for a total duration of 6.4 s with time separation of  $T_o=8$  ms. The total duration is long enough to resolve the evolution from laminar to turbulent, while the time separation is fine enough to capture the temporal variation. The processed velocity fields are originally in Cartesian system, and they are later transformed into cylindrical coordinate system, commonly used in vortex ring or round jet study. The current coordinate systems are shown in figure 3. The azimuthal vorticity  $\omega_\theta$  distribution along ring radius in the first snapshot is shown in figure 4, where the axial velocity distribution is also overlaid. The peak of  $\omega_\theta$  appears at  $r=22.5$  mm, which is taken as the ring radius  $R$ . The vortex core radius  $\delta$  is defined as the distance between the torus and the location where maximum axial velocity is reached, it is  $\delta=8.4$  mm. The definitions of  $R$  and  $\delta$  are also shown in figure 3. The vortex ring therefore has a slenderness ratio of  $\varepsilon = \delta/R = 0.37$ . The slenderness ratio is useful in predicting the wavenumber  $n$  associated with transition. An empirical formulation for wavenumber estimation is  $n \approx 2.26/\varepsilon$  [6]. The present vortex ring then has a wavenumber of 6. In the following data presentation and result discussion, the ring radius  $R$  and the measurement time separation  $T_o$  are adopted as length and temporal scaling parameter.

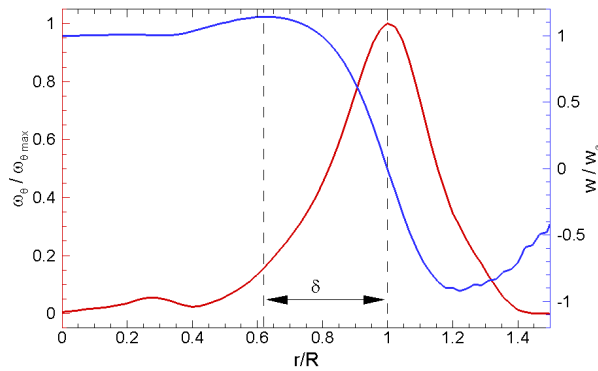


Fig. 4 Distribution of azimuthal vorticity  $\omega_\theta$  (red curve) and axial velocity  $w$  (blue curve) along radius.

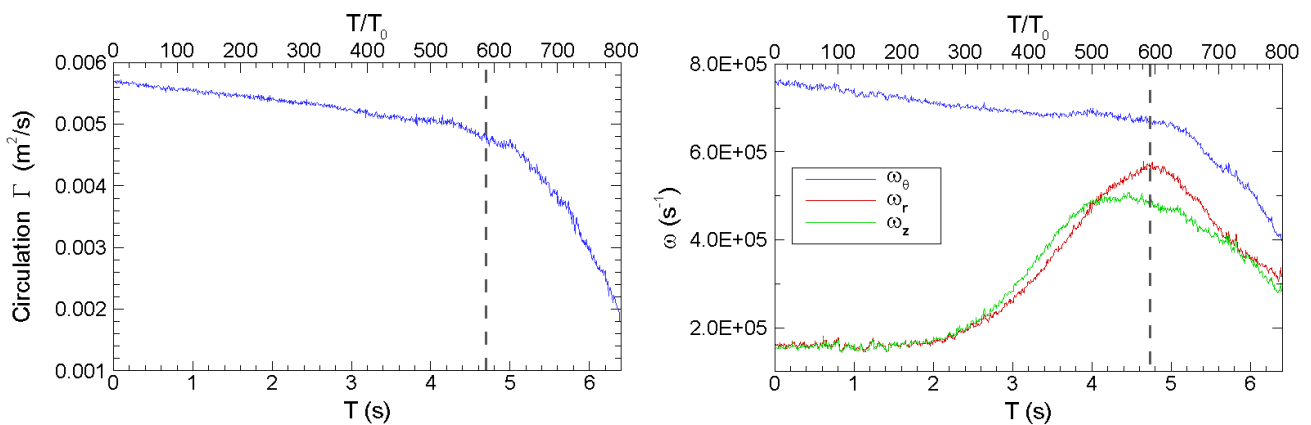


Fig. 5 Evolution of circulation (a) and vorticity components (b)

The variation of the circulation magnitude along the evolution gives an indication of each development phase. The vortex ring initially has circulation of  $\Gamma_0 = 0.0057 \text{ m}^2/\text{s}$ . The decay of circulation, as visualized in figure 5(a), can be divided into two major phases. The first phase is from the beginning to  $T = 4.7 \text{ s}$  or  $590T_0$ . It is featured by a steady decay. At the end of the first stage 82% of the initial magnitude still remains. However, a “circulation catastrophe” is exhibited in the next phase, where more than 50% of the initial circulation is rapidly lost within 1.8 s or  $210T_0$ . The dramatic drop is due to the dissipation after the vortex ring turns into turbulent. The evolution of each vorticity component as shown in figure 5(b) offers further details in the two phases. The quantity of vorticity component at each snapshot is calculated through summation of each component within the entire volume. The azimuthal component  $\omega_\theta$  experiences two stages of decay, similar as circulation. The magnitudes of the radial  $\omega_r$  and axial vorticity  $\omega_z$  components remain minimum before  $T = 2 \text{ s}$  or  $250T_0$ . Generation of both components takes place as soon as the ring enters the transition phase characterized by secondary vortical generation associated with flow instability. The axial vorticity  $\omega_z$  reaches its maximum at  $T/T_0 = 500$ , while radial vorticity  $\omega_r$

peaks with a slight delay at  $T=590T_0$ , coinciding with the beginning of ‘circulation catastrophe’. As a result, the initiation of turbulent phase can also be represented as the peak of radial vorticity. So far the evolution of the vortex ring is divided into laminar ( $T/T_0 = 0\sim 250$ ), transition ( $T/T_0 = 250\sim 590$ ) and turbulent phase ( $T/T_0 > 590$ ). The fluid dynamics properties of the present vortex ring are summarized in table 3.

**Table 3** Fluid dynamic properties of the vortex ring

Parameter	Quantity
Ring radius	$R = 22.5 \text{ mm}$
Core radius	$\delta = 8.4 \text{ mm}$
Slenderness ratio	$\varepsilon = \delta/R = 0.37$
Wavenumber	$n = 6$
Initial circulation	$\Gamma_0 = 0.0057 \text{ m}^2/\text{s}$
Piston-based Reynolds number	$Re_p = 4650$
Laminar life span	$250T_0$
Transition lift span	$340T_0$

### 3.2 Evolution of the vortex ring

The vortical structure along the evolution process is going to be addressed in this section by taking advantage of the three-dimensional measurement technique. 7 snapshots from  $T=100T_0$  to  $700T_0$  are selected to represent the ring at the laminar ( $100, 200T_0$ ), transition ( $300, 400, 500T_0$ ) and turbulent ( $600, 700T_0$ ) phases respectively.  $Q$ -criterion is used for vortex identification.

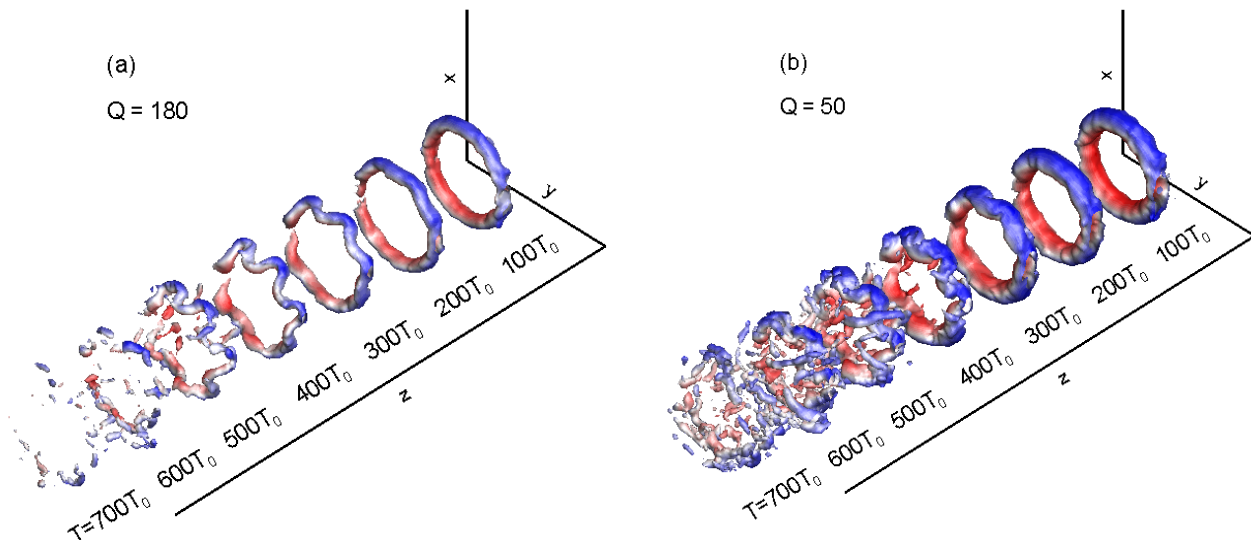


**Fig. 6** Evolution of the vortex ring in laminar phase ( $100T_0, 200T_0$ ), transition phase ( $300T_0, 400T_0, 500T_0$ ), turbulent phase ( $600T_0, 700T_0$ ) visualized by  $Q=180$  (a) and by  $Q=50$  (b). The isosurface is colored by axial velocity magnitude.

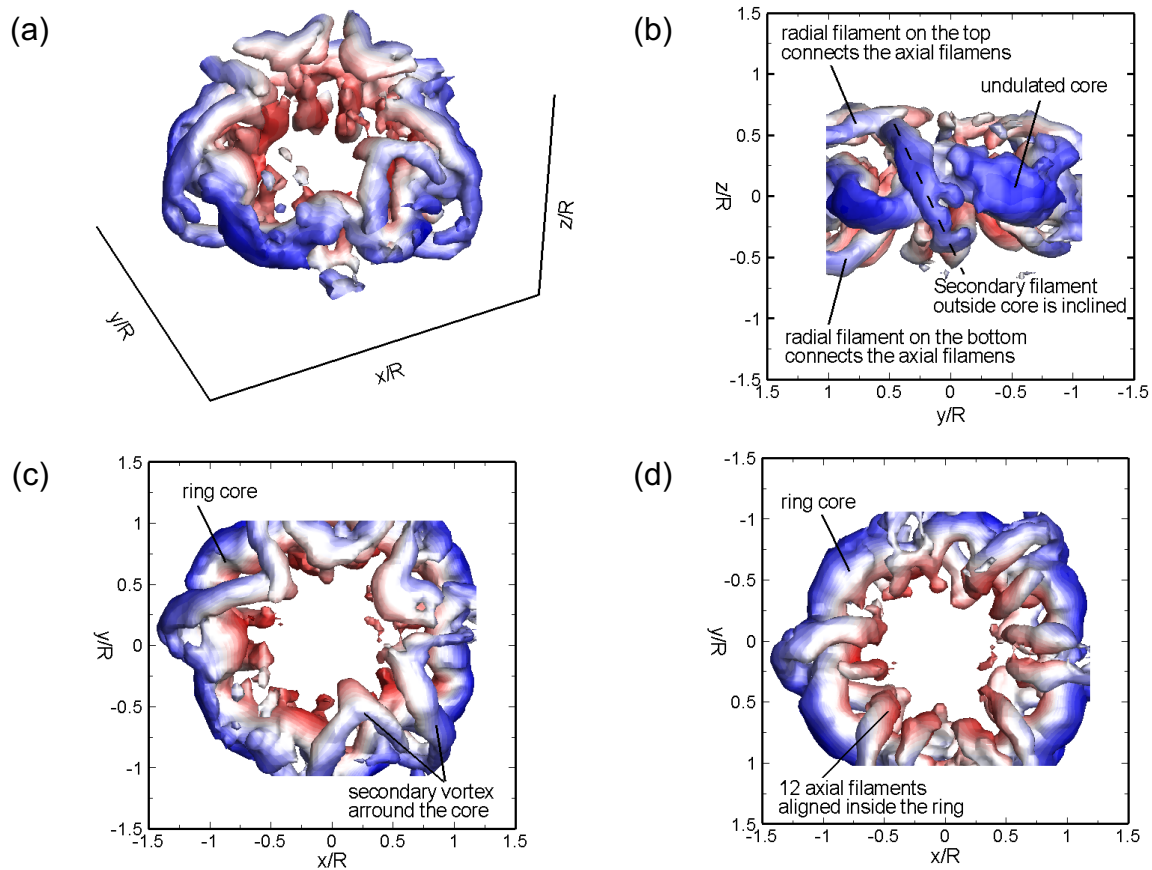


**Fig. 7** Vortex ring at  $T/T_0=500$  represented by isosurface of  $Q=30$ . The vortex surface is colored by the magnitude of axial velocity: (a) isometric view, (b) side view, (c) top view, (d) bottom view.

A large value of  $Q=180$  is first chosen to visualize the evolution of the ring core, see figure 6(a). The torus remains a smooth ring in the laminar phase. Undulation of the ring core can be observed at  $300T_0$ , nearly at the beginning of transition. It results in the development of 6 standing waves along the ring azimuth, which confirms the empirical estimation. The wave amplitude grows gradually in downstream propagation. Upon entering the turbulent phase from  $T/T_0=600$ , the ring core is no longer a complete torus and starts to break up into fragments. Since the torus is subject to rapid decay in circulation in the turbulent phase, it is not surprising that only tiny fragments can be observed at  $T/T_0=700$ .

In order to visualize the ring core as well as the secondary vortical structures simultaneously, the evolution process is also represented by a smaller value of  $Q=50$  as shown in figure 6(b). A thicker core is represented by  $Q=50$ , which exhibits identical behavior. More importantly, generation and growth of axial and radial vortex filaments are obvious in the transition phase. As the secondary vortices can only be visualized when smaller value of  $Q$  is used, it can be inferred that they are

weaker than the ring core. The axial secondary filaments sustain in early turbulent phase at  $T/T_0=600$ . However, they eventually dissipate together with the core into turbulent eddies in much smaller size.

The ring in the late transition at  $T/T_0=500$  is selected and plotted individually in figure 7 for the purpose of revealing its vortical organization. The secondary vortices extend in both axial and radial directions and wrap around the ring core. The portion located outside the ring core as shown in figure 7(b) is inclined from the axis. This vortex is usually referred as halo vortex, which further extends radially above and below the ring core and finally connects with axial filaments inside the ring. The secondary vortices above the ring are shown in figure 7(c). The pattern resembles hexagram, although one angle is missing due to the weak strength in that corner. The number of the axial filaments within the torus is 12 and is clearly visualized in figure 7(d).

### 3.3 The median plane in the transition phase

The present section explores the flow features associated with transition in the median plane at  $z=0$ , where the most prominent signature of transition is contained. Note that the location of the median plane is illustrated in figure 3. Evolution of the axial vorticity component in the median plane is first shown, see the contours of  $\omega_z$  in figure 8. The axial vorticity component is important because the secondary vortices are most evident in axial direction. Moreover, the ring core starts to obtain axial vorticity magnitude initially when torus undulation begins. The distribution of  $\omega_z$  features three concentric rings: the central one belongs to the ring core, while the outer and inner layers represent the secondary vortex filaments. A striking feature of ring-shaped organization is the packets of  $\omega_z$  with alternating signs, which suggests the  $180^\circ$  phase difference between the neighboring filaments. In the early and middle stages of transition, namely  $300T_0$  and  $400T_0$ , the vorticity packets align strictly along the three rings. The spacing between packets in the 1<sup>st</sup>, 2<sup>nd</sup> and 4<sup>th</sup> quarters is compact, while that in the 3<sup>rd</sup> quarter is coarser. Although similar three-layer structure and opposing patterns can be observed in the late transition ( $500T_0$ ), in-plane motion of the packets already takes place and gives rise to distortion.

The radial velocity component is also of great interest as it represents the secondary flow motion caused by vortical activity. The distribution of  $u_r$ , see figure 9, is also organized in focused patterns, which are aligned along concentric rings. Again, regularity of the pattern is not well followed in the 3<sup>rd</sup> quarter. For example, the packet containing positive  $u_r$  does not show up in the 3<sup>rd</sup> quarter in  $300T_0$  and  $400T_0$ . Therefore the undulation in the 3<sup>rd</sup> quarter is delayed comparing to the other positions of the ring. The 12 packets containing positive and negative radial velocity are produced in the late transition at  $500T_0$ , however, they tend to meander within the plane.

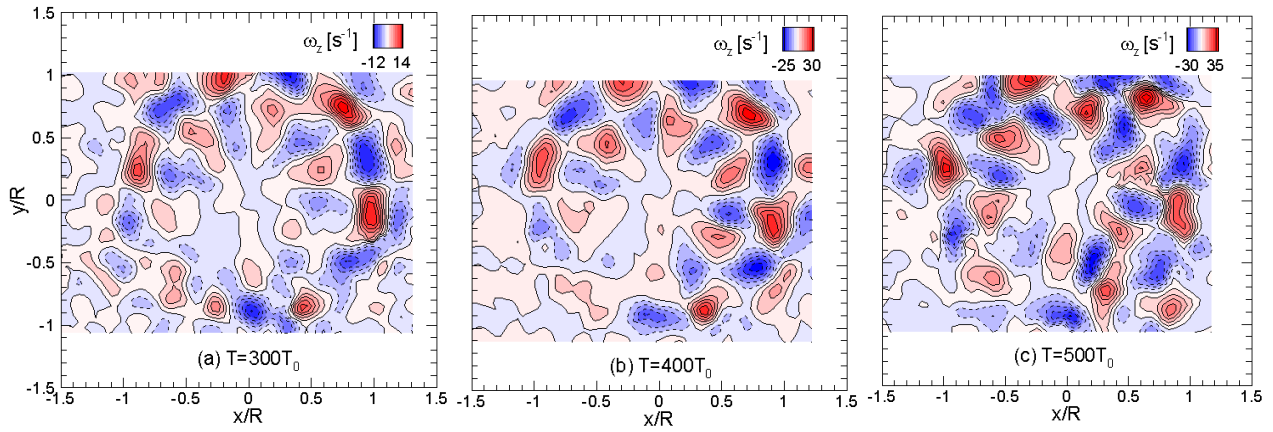


**Fig. 8** Contour of axial vorticity  $\omega_z$  in the median plane  $z=0$  at  $T=300T_0$  (a),  $400T_0$  (b),  $500T_0$  (c).

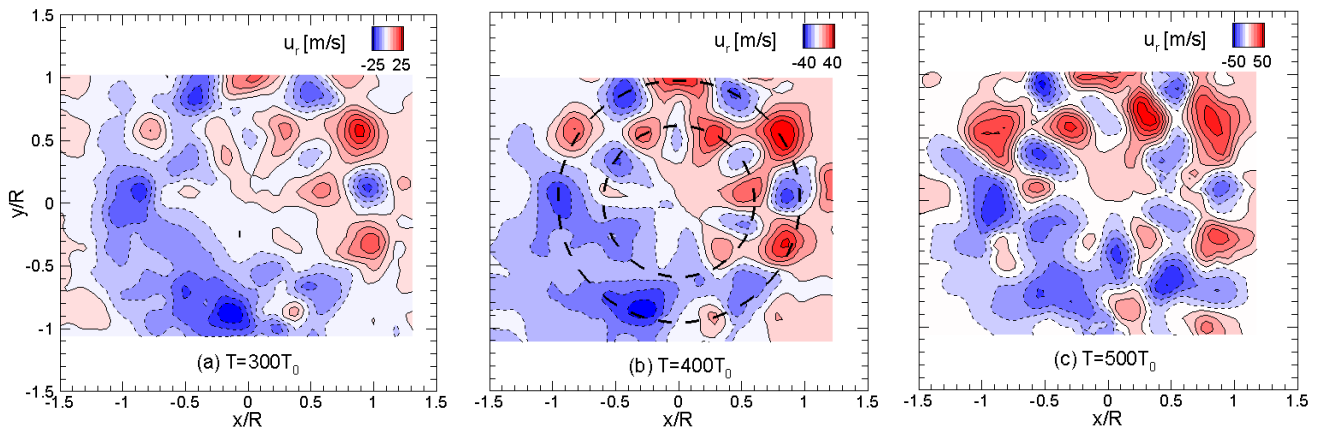


**Fig. 9** Contour of radial velocity  $u_r$  in the median plane  $z=0$  (a)  $300T_0$ , (b)  $400T_0$ , (c)  $500T_0$ .

The present measurement technique enables to examine the temporal variation of the radial velocity spectrum along the ring azimuth, which adds further insight into the development of the instability in the ring. The radial velocity component along two circles with radii  $r/R=0.6$  and  $1.0$  are first extracted from the volumetric flow field. These two circular locations go through the major and inner ring respectively. The extracted radial velocity are then stacked along the temporal axis as shown in temporal-azimuthal plane in figure 10. In the initial phase till about  $300T_0$ , no prominent pattern can be seen. Stripes with altering  $u_r$  start to develop later on and they grow throughout the transition phase towards  $600T_0$ , which confirms the phase classification based on the vorticity growth. From  $600T_0$  onward, the stripes do not remain straight and divided. Instead, they meander and merge, which signals the turbulent activity.

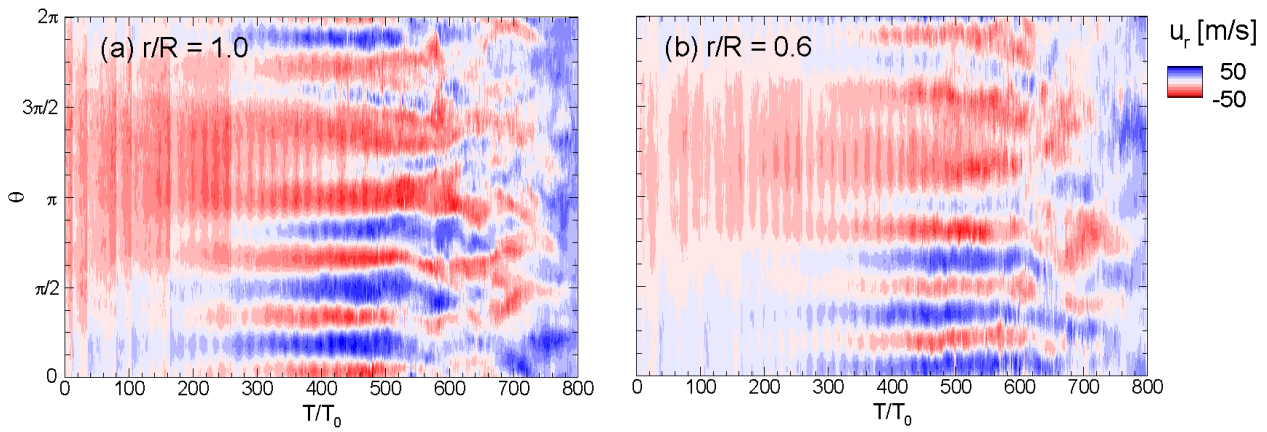


**Fig. 10** Temporal evolution of the radial velocity extracted from circle with radius of (a)  $r/R=1.0$  (b)  $r/R=0.6$ .

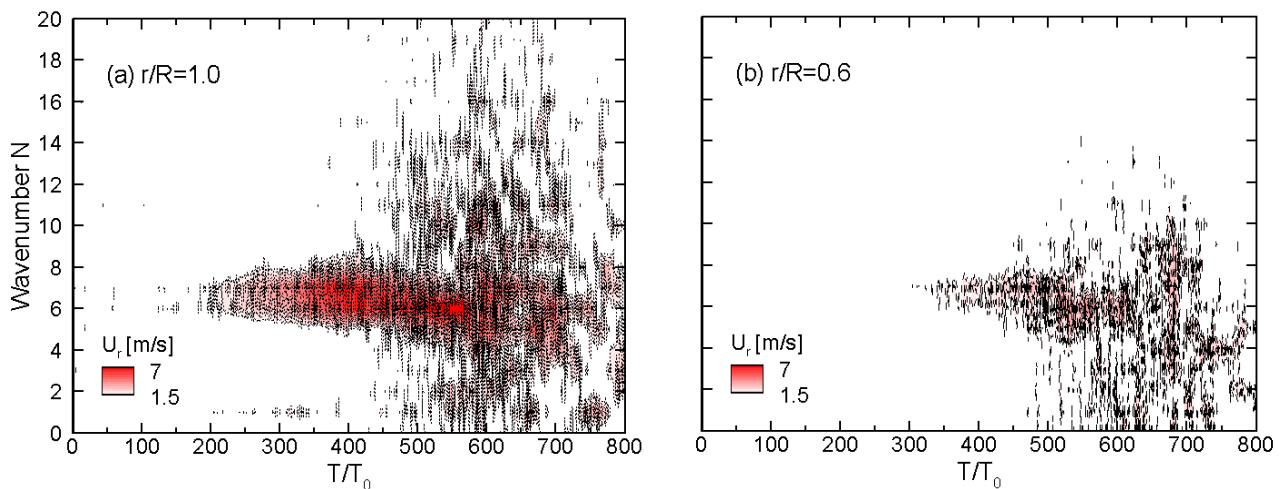


**Fig. 11** Temporal evolution of wavenumber for the radial velocity extracted from circle with radius of (a)  $r/R=1.0$  (b)  $r/R=0.6$ .

FFT of the radial velocity distribution in figure 10 is carried out and the decomposed radial velocity amplitudes are presented in the temporal-wavenumber space, intending to reveal the temporal evolution of the embedded wavenumber. In the circular location at  $r/R=1.0$ , namely the center of ring core, peaks belong to dual wavenumbers of 6 and 7 can be observed from  $200T_0$  to about  $500T_0$ , suggesting that the major portion of transition is actually dominated by two wavenumbers. However, the peak of  $N=7$  starts to decay from about  $500T_0$ , which means the late transition is affected primarily by single wavenumber of  $N=6$ , although there are a few minor weak peaks corresponding to  $N>10$ . Once the turbulence phase is approached, the focused peak become scattered to a broad range of wavenumbers with less amplitude. Moreover, they are intermittent in temporal scale.

The spectrum of the secondary activity is inspected through the circular location at  $r/R=0.6$ , see figure 11(b). Peaks of  $N=6$  and 7 are evident in the transition phase, however, with reduced magnitude than that in the core. The peak of  $N=7$  does not emerge from about  $320T_v$ , when the axial vorticity is produced. In the late transition from  $500T_v$ , the secondary activity is taken over by wavenumber of  $N=6$ . Similarly, broader and intermittent wavenumbers appears in the turbulent phase.

#### 4 Conclusion

The present experimental work examines the temporal evolution of a vortex ring. The observation takes advantages of the time-resolved 3D measurement technique. The ring evolution is divided into laminar, transition and turbulent phases based on the variation of the vorticity components as well as the ring circulation. In the laminar phase, the vortex ring undergoes steady decay in circulation however no significant deformation happens. The transition phase has a duration twice of the laminar phase. It features the undulation of ring torus and generation of secondary vortical filaments surrounding the torus. Analysis on the axial vorticity and radial velocity in the median plane provides more details of the flow pattern in the transition phase. Both quantities are organized in concentric patterns with alternating signs. However, along each layer of the ring pattern, all the packets are not evenly aligned, instead they tend to be compact in one direction resulting the packets on the opposite corner with larger spacing and weaker intensity. Spectrum analysis on the radial velocity along the circles provides further insight throughout the evolution. It has been revealed that radial velocity along the ring core feature dual wavenumbers of 6 and 7 in transition phase, however, wavenumber  $N=6$  is more dominant in the late transition. The inner ring location, where the secondary vortical activity takes place, is initially affected by  $N=6$  while  $N=7$  takes over in the late transition. The final turbulent phase is dominated by a broad band of wavenumbers, which are weaker intensity and also intermittent in duration.

#### References

- [1] Archer P, Thomas T, Coleman G (2008) Direct numerical simulation of vortex ring evolution from the laminar to the early turbulent regime. *J Fluid Mech* 598:201-226.
- [2] Dazin A, Dupont P, Stanislas M (2006) Experimental characterization of the instability of the vortex ring Part I: linear phase, *Exp Fluids* 40:383-399.
- [3] Pointz B, Sastuba M, Bruecker C, Kitzhofer J (2012), Volumetric velocimetry via scanning back-projection and least-squares-matching algorithms of a vortex ring, 16<sup>th</sup> Int Symp on Applications of Laser Techniques to Fluid Mechanics.

- [4] Brücker Ch (1995) Digital-particle-image-velocimetry (DPIV) in a scanning light-sheet: 3D starting flow around a short cylinder, *Exp Fluids* 19:255–263.
- [5] Elsinga G, Scarano F, Wieneke B, van Oudheusden B (2006) Tomographic particle image velocimetry, *Exp Fluids* 41:933-947.
- [6] Pointz B, Sastuba M, Bruecker C (2016) 4D visualization study of a vortex ring lift cycle using modal analysis, *J Vis* 19:237-259.
- [7] Shariff K, Verzicco R, Orlandi P (1994) A numerical study of 3D vortex ring instabilities: viscous corrections and early nonlinear stage. *J. Fluid Mech* 279:351-375.